Chemical Engineering Journal 347 (2018) 889–899

Contents lists available at ScienceDirect

Chemical Engineering Journal

journal homepage: www.elsevier.com/locate/cej

Design and synthesis of tube-in-tube structured NiO nanobelts with superior electrochemical properties for lithium-ion storage

Se Hwan Oh[a,1], Jin-Sung Park[b,1], Min Su Jo[a], Yun Chan Kang[b,*], Jung Sang Cho[a,*]

[a] Department of Engineering Chemistry, Chungbuk National University, Chungbuk 361-763, Republic of Korea
[b] Department of Materials Science and Engineering, Korea University, Anam-Dong, Seongbuk-Gu, Seoul 136-713, Republic of Korea

HIGHLIGHTS

- Novel 1-D tube-in-tube structured NiO nanobelts were synthesized by electrospinning process.
- Influence of calcination temperature on the formation of nanobelts with various morphologies was investigated in detail.
- The chemicals that optimized surface tension and viscosity of the aqueous solution enabled stable electrospinning process.
- Unique structured NiO tube-in-tube nanobelts showed excellent lithium-ion storage performances.

ARTICLE INFO

Keywords:
Tube-in-tube
Nickel oxide
Anode
Lithium ion battery
Electrospinning

ABSTRACT

Novel 1-D tube-in-tube structured NiO nanobelts were prepared by electrospinning process and subsequent one-step thermal treatment process. Nanobelt structured 1-D composite was electrospun from an aqueous solution containing poly(vinylpyrrolidone), citric acid, and dextrin which synergistically contributed to morphology control. The chemicals that optimized surface tension and viscosity of the aqueous solution enabled stable electrospinning process. Especially, dextrin played an important role in stable nanobelt formation due to its hygroscopic nature. During one-step oxidation process, the polymer composited nanobelt turned into carbon-free NiO@void@NiO tube-in-tube structured nanobelt by repeated combustion and contraction processes and Ostwald ripening mechanism. NiO tube-in-tube nanobelt prepared at 400 °C showed superior lithium-ion storage performances compared to those of NiO-C nanobelt and porous NiO nanobelt obtained at 300 and 500 °C, respectively. The discharge capacity of the tube-in-tube structured nanobelts after the 200th cycle at a current density of 1.0 A g^{-1} was 992 mA h g^{-1}. Also, high discharge capacity of 531 mA h g^{-1} at a current density of 10.0 A g^{-1} proved its excellent power density. High structural stability and morphological benefits of tube-in-tube nanobelts resulted in superior lithium storage performance.

1. Introduction

Transition metal oxides have been widely studied as promising anode materials for lithium ion batteries (LIBs) because of their high capacities, which exceed those of commercial carbonaceous materials [1–9]. Among transition metal oxides, NiO has received great research interest for its low density, high abundance, and nontoxicity [10–14]. However, NiO has poor electronic conductivity like other transition metal oxides, which results in disturbance of conduction paths for both electron and Li^+ ion [15–17]. These are considered as critical obstacles for LIBs and result in poor rate capability and cycling stability [15–17]. Therefore, various NiO materials with hollow and porous morphologies have been developed to achieve excellent electrochemical properties by improving their structural stabilities during the repeated lithium insertion and deinsertion processes [18–26]. Kang et al. synthesized yolk-shell and single-crystalline NiO powders by continuous one-pot spray pyrolysis and flame spray pyrolysis, respectively [18]. Yolk-shell-structured NiO powders showed higher discharge capacity of 951 mA h g^{-1} than that of the single-crystalline cubic NiO nanopowders (416 mA h g^{-1}) after 150 cycles. Synthesis of hierarchical 3D-NiO microspheres with ultra-thin porous nanoflakes by chemical co-precipitation method and subsequent thermal treatment was reported by Seo et al. [25]. The capacity of NiO microspheres retained 795 mA h g^{-1} after 150 cycles at 0.5 C. Liu et al. synthesized highly ordered mesoporous NiO by a nanocasting method using mesoporous silica as the hard template [26]. The powders obtained using this

* Corresponding authors.
E-mail addresses: yckang@korea.ac.kr (Y.C. Kang), jscho@cbnu.ac.kr (J.S. Cho).
[1] These authors contributed equally to this work.

https://doi.org/10.1016/j.cej.2018.04.156
Received 12 February 2018; Received in revised form 10 April 2018; Accepted 23 April 2018
Available online 24 April 2018
1385-8947/

method had specific capacity of 680 mA h g^{-1} after 50 cycles at 0.1 C, which was much higher than that of the commercial bulk NiO (188 mA h g^{-1}).

Recently, one-dimensional (1-D) nanostructures have been recognized as the most desirable materials for use in energy storage [27–35]. Their unique structures provide enhanced surface-to-volume ratios, short Li^+ ionic transport lengths, and efficient 1-D electron transport along their longitudinal directions [29,30]. Therefore, the application of 1-D geometries to the hollow nanostructure has been considered attractive for use in LIBs. Cho et al. prepared NiO nanofibers composed of hollow NiO nanospheres by electrospinning method and compared the lithium storage properties with those of porous NiO nanofibers [35]. The nanofibers composed of hollow nanospheres showed superior discharge capacity of 707 mA h g^{-1} than that of porous one (206 mA h g^{-1}) for the 250th cycle at a current density of 1.0 A g^{-1}.

This paper proposes a simple and highly efficient preparation method for NiO tube-in-tube-structured nanobelts by electrospinning process and subsequent heat-treatment process. To the best our knowledge, preparation process for tube-in-tube-structured transition metal oxide nanobelts has not yet been researched. Also, there are not many reports on nanofibers electrospun from aqueous solution due to difficulty in obtaining the suitable degree of viscosity and surface tension. The first introduction of dextrin to aqueous electrospinning solution enabled the formation of nanobelt due to its hygroscopic nature. Addition of poly(vinylpyrrolidone) increased viscosity and lowered surface tension. Citric acid further lowered surface tension to a certain degree suitable for stable electrospinning. During subsequent oxidation, sudden combustion of carbonized electrospun nanobelt turned it into NiO-C@void@NiO fiber-in-tube morphology. Continuous heating yielded NiO tube-in-tube structure by Ostwald ripening. Electrochemical properties of tube-in-tube structured NiO nanobelts were compared with those of filled NiO-C nanobelt and porous NiO nanobelts prepared at different post-treatment temperatures.

2. Experimental

2.1. Synthesis of NiO nanobelts with tube-in-tube structure

NiO nanobelts with tube-in-tube structure were prepared using electrospinning process and subsequent thermal-treatment. First, composite nanobelts comprising nickel(II) nitrate tetrahydrate [$Ni(NO_3)_2{\cdot}4H_2O$, Junsei, 98.0%], poly(vinylpyrrolidone) [PVP, Mw: 1,300,000, Sigma Aldrich], citric acid [$C_6H_8O_7$, Samchun Chemicals, 99.5%], and dextrin [$(C_6H_{10}O_5)_n$, Samchun Chemicals] were electrospun. The electrospinning precursor solution was prepared by dissolving 2.0 g of PVP and 10.0 g of dextrin in a mixed solution containing 20 mL of deionized water and 2.0 g of citric acid with vigorous stirring for 3 h. Then, 3.0 g of nickel(II) nitrate tetrahydrate was added to the above solution. The prepared solution was loaded into a plastic syringe equipped with a 27-gauge stainless steel nozzle. The solution was subsequently ejected at a flow rate of 0.1 mL h^{-1} and electrospun onto a drum collector constantly heated at 180 °C. During the electrospinning process, the distance between the tip and the collector was maintained at 15 cm, while the rotation speed of the drum was 150 rpm. The applied voltage between the collector and the syringe tip was 25 kV. The resulting nanobelts comprising $Ni(NO_3)_2$-PVP-dextrin-citric acid were stabilized at 100 °C under air for 3 h. Subsequently, the nanobelts were heat-treated at 300, 400, and 500 °C for 3 h under air atmosphere. For simplicity, the resulting NiO nanobelts obtained after heat-treatment at 300, 400, and 500 °C are referred to as “NiO/C-300”, “NiO-400”, and “NiO-500” respectively.

2.2. Characterization techniques

The microstructures of the samples were examined by field-emission scanning electron microscopy (FE-SEM, ULTRA PLUS, ZEISS) and field-emission transmission electron microscopy (FE-TEM, JEOL, JEM-2100F). In addition, their phase analysis was evaluated by X-ray diffractometry (XRD, D8 Discover with GADDS, The Bruker) using Cu K_α radiation (λ = 1.5418 Å). The Fourier transfer infrared (FT-IR) spectra were obtained by a JASCO FT-IR 480 Plus spectrophotometer. X-ray photoelectron spectroscopy (XPS, Thermo Scientific K-Alpha) with a focused monochromatic Al K_α at 12 kV and 20 mA was used to analyze the composition of the specimens. The surface areas of the nanobelts were measured using the Brunauer–Emmett–Teller (BET) method using N_2 as the adsorbate gas. Thermogravimetric (TG) analysis was performed using a Pyris 1 TGA (Perkin Elmer) within a temperature range of 25–700 °C at a heating rate of 10 °C min^{-1} under air.

2.3. Electrochemical measurements

The capacities and cycle properties of the samples were measured using 2032-type coin cells. The cell electrodes were prepared using slurry consisting of 70 wt% active anode material, 20 wt% carbon black (Super-P) as a conductive material, and 10 wt% binder composed of sodium carboxymethyl cellulose (CMC) on a copper foil. Lithium metal and microporous poly(propylene) film were used as the counter electrode and separator, respectively. The electrolyte was created by dissolving 1 M $LiPF_6$ in a mixture of fluoroethylene carbonate and dimethyl carbonate (FEC/DMC, 1:1 v/v). The entire cell was assembled in an argon atmosphere in a glove box. The charge/discharge characteristics of the samples were measured at various current densities in the voltage range of 0.001–3.0 V. The size of the negative electrode containing the NiO nanobelts was 1.4 cm × 1.4 cm, and the mass loading was approximately 0.84 mg cm^{-2}. Cyclic voltammetry measurements were performed at a scan rate of 0.1 mV s^{-1} between 0.001 and 3.0 V. Electrochemical impedance spectra of NiO nanobelts were analyzed in the frequency range between 100 kHz and 10 MHz at room temperature with a signal amplitude of 5.0 mV.

3. Results and discussion

Morphologies of the as-spun composite electrospun from aqueous solutions containing nickel salt with PVP, dextrin, citric acid, and PVP/citric acid are shown in Fig. 1. In this study, in order to obtain uniform nanobelts, effects of each additive and their combination on morphology control during electrospinning process were demonstrated in detail. Fig. 1a shows the nickel salt-polymer composite without specific morphology, electrospun from aqueous solution containing PVP. It is generally known that surface tension of electrospinning solution should be lowered to fabricate 1-D morphology without bead formation. When PVP is dissolved in water, surface tension decreases slightly while viscosity rises. In order to obtain low enough surface tension for electrospinning by dissolving PVP in distilled water, it must be accompanied by a large increase in viscosity that blocks the stable electrospinning process [36,37]. In case of aqueous solution containing 10 wt % PVP, capillary breakup of electrospinning jets occurred due to high surface tension of the solution. As a result, droplets were generated and solidified on the drum collector surface, forming composite with random morphology. In search of organic compound that can lower the surface tension effectively, dextrin was chosen as a candidate [38]. In Fig. 1b, random morphology was observed for the nickel salt composite electrospun from a solution containing dextrin. Dextrin is highly soluble in water and contains many functional groups with ability to form hydrogen bonding with water. As a result, existence of dextrin blocks the formation of hydrogen bonding between water molecules, and thus can lower the surface tension. However, viscosity increase was not possible for dextrin is an oligomer with low molecular weight. It was not viscous enough and resulted in random shape. Electrospun nickel salt composite from aqueous solution containing citric acid is presented in Fig. 1c. Citric acid plays the role of lowering surface tension to some extent [39]. However, it does not satisfy the required viscosity and

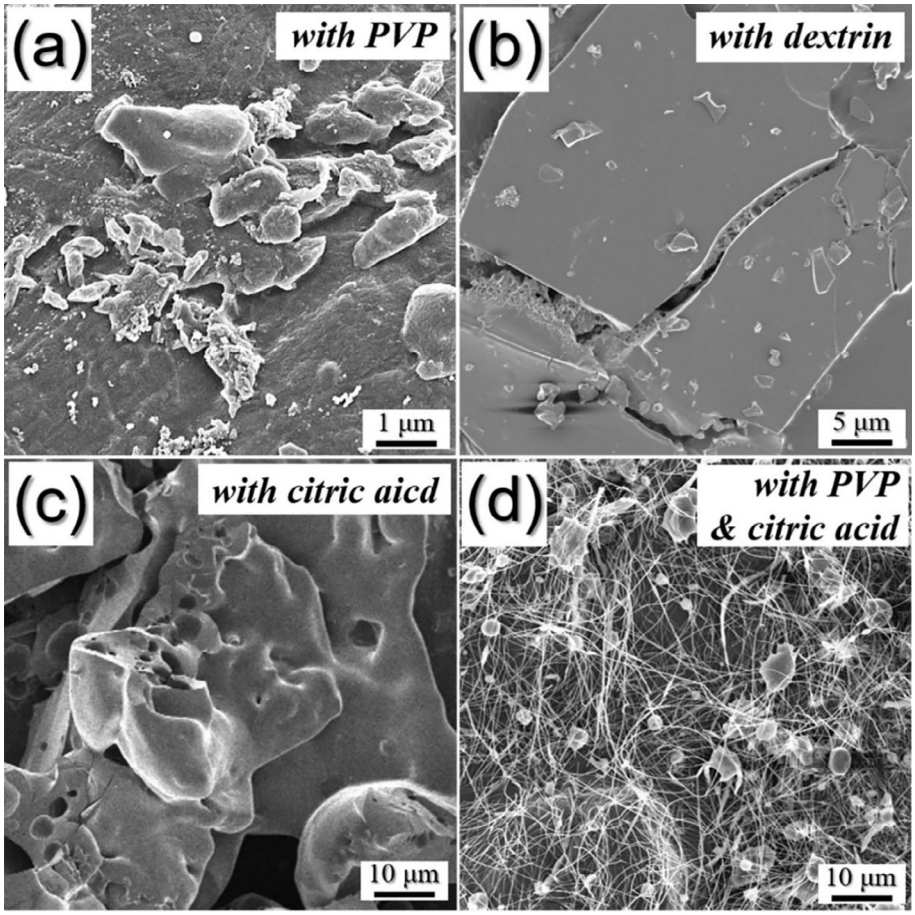

Fig. 1. FE-SEM images of composites electrospun from aqueous solutions containing nickel salt with (a) PVP, (b) dextrin, (c) citric acid, and (d) PVP and citric acid.

surface tension for obtaining nanofiber and thus resulted in amorphous morphology. Coexistence of fibers and beads was observed for the composite material electrospun from solution containing PVP and citric acid as shown in Fig. 1d. Both PVP and citric acid lowered the surface tension of water to some extent. However, there exists a limit to how much surface tension can be reduced by adding citric acid. As a result, due to the still high surface tension of solution, beads were formed as well as nanofibers due to intermittent capillary breakup of electrospinning jets. Finally, as-spun fibers were in the form of nanobelt when electrospun from aqueous solution containing PVP, citric acid, and dextrin in the optimum ratio, as can be seen in Fig. 2a.

Carboxyl groups in citric acid triggers the formation of hydrogen bonding between dextrin and PVP, resulting in blend solution (Scheme 1). As mentioned above, PVP, citric acid, and dextrin played the roles of lowering surface tension. Furthermore, PVP increased viscosity to a certain point suitable for stable electrospinning. When the solution was subjected to a high voltage, jet was formed and could be maintained over the entire electrospinning process. Solidification occurred only at the exterior of the jet because solvent located at the centre could not be volatilized due to the high concentration of the electrospinning solution and remained as liquid. Nanobelt morphology was obtained due to the surface collapse from the impact electrospun jet received on hitting the drum collector. This was attributed to the soft interior of the jet [40,41]. The temperature of the drum collector (180 °C) enabled the crosslinking reactions between citric acid and dextrin, and increased the mechanical strength of the exterior jet; 3 carboxyl groups in citric acid reacted with 3 hydroxyl groups in dextrin and formed ester as shown in Scheme 1. The crosslinking reactions between citric acid and dextrin are further confirmed by evaluating the FT-IR spectrum of the electrospun nanobelt in Fig. 2b. It revealed two peaks near 3400 cm^{-1} and 1735 cm^{-1}; peak near 3400 cm^{-1} could be attributed to O–H stretching vibrations from hydroxyl groups in dextrin and carboxyl groups in citric acid, whereas peak at 1735 cm^{-1} corresponds to the ester group formed by crosslinking of dextrin and citric acid at 180 °C [42,43]. Dextrin with hygroscopic properties played an important role in stable nanofiber formation even in highly humid atmosphere. Solidification occurred at the exterior part, forming jet with soft interior and hard exterior. On impact with the drum collector, jet experienced surface collapse and nanobelt morphology was obtained. After nanobelt formation, esterification crosslinking of dextrin and citric acid at 180 °C lowered the solubility of nanobelt in water [42]. As a result, nanobelt morphology could be maintained at ambient condition. Average width and aspect ratio were 0.8 μm and 4:1, respectively, and rectangular cross section in the inset image of Fig. 2a could be clearly observed. Stabilization under 100 °C formed composite nanobelts with an amorphous structure. The corresponding XRD pattern in Fig. S1a also revealed that amorphous composite nanobelts were formed. TGA curve of the electrospun nanobelt in Fig. S1b reveals that PVP, dextrin, and citric acid decompose fully at temperature near 300 °C.

The morphologies of the nanobelts post-treated at temperatures of 300, 400, and 500 °C are shown in Figs. 3–5. The morphology of the nanobelts post-treated at a relatively lower temperature of 300 °C under an air atmosphere is shown in Fig. 3. The overall morphology of the nanobelts was maintained even after heat-treatment as can be seen in the SEM and TEM images in Fig. 3a and b. Ultrafine nickel oxide nanocrystals formed from decomposition of nickel salt could be observed in the TEM images in Fig. 3c and d. From the unclear rings in SAED pattern in Fig. 3e, it was further confirmed that NiO-C nanobelts had ultrafine nanocrystals, which is in line with the XRD data in Fig. S2. Temperature was not high enough to remove carbon by burning, which

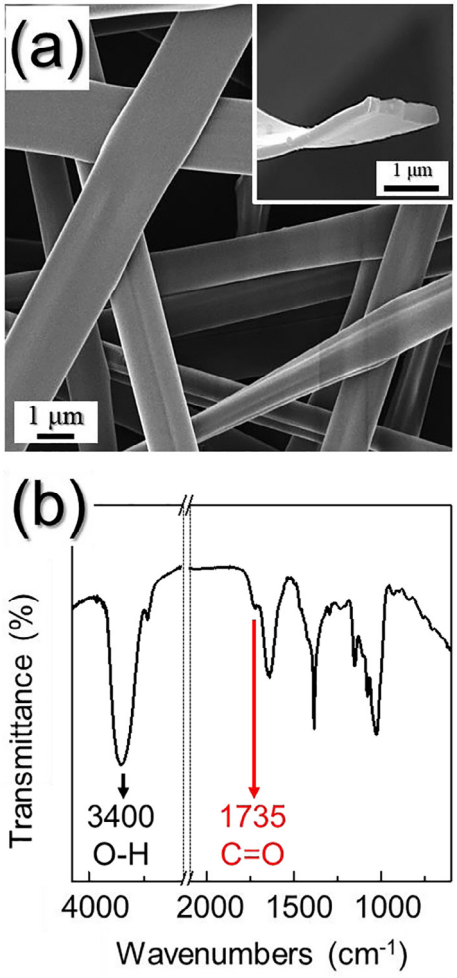

Fig. 2. (a) SEM image, (b) FT-IR spectrum of the as-spun $Ni(NO_3)_2$-PVP-dextrin-citric acid composite nanobelts prepared by electrospinning process.

is in agreement with the TG curve in Fig. S3a, in way that 15% weight loss was observed for NiO/C-300. The elemental mapping images in Fig. 3f reveal the uniform distributions of the Ni, O, and C components all over the nanobelt. Therefore, it is confirmed that the filled structured composite nanobelts consisting of ultrafine NiO nanocrystals distributed within incompletely decomposed carbon were obtained after heat treatment at 300 °C.

Oxidation of the composite nanobelt at a temperature of 400 °C yielded tube-in-tube structured NiO nanobelt as shown in Fig. 4. The complete carbonization and sudden combustion of carbon in the filled structured NiO-C composite nanobelts resulted in the formation of NiO@NiO-C core-shell nanobelt and subsequently NiO-C@void@NiO fiber-in-tube morphology was formed. Complete combustion of carbon yielded filled NiO@void-NiO nanobelt as an intermediate structure. Continued heating led to Ostwald ripening, resulting in monophasic NiO nanobelts with tube-in-tube structure shown in Fig. 4a–c. The shell thickness of the NiO nanobelts with tube-in-tube structure was approximately 25 nm. A clear void space existing in the nanobelts is observed in the SEM and TEM images. Void spaces within the structure can alleviate volume changes during lithiation/delithiation process, increasing the structural stability. Furthermore, Li^+ ion diffusion length is decreased owing to the structural merits of tube-in-tube structure. Pure crystal phase of NiO phase was confirmed by XRD shown in Fig. S2. By applying the Scherrer equation to the (012) cubic NiO peak, the mean crystallite size of NiO-400 were calculated as 26 nm. The high resolution TEM images revealed lattice fringes separated by 0.21 nm, which correspond to the (200) lattice plane of cubic NiO, as shown in the inset image of Fig. 4d. In TGA curve (Fig. S3b), no weight loss of the samples under air atmosphere was observed, indicating complete combustion of carbon during the post-treatment process. Even though the oxidation temperature was low as 400 °C, carbon wasn't observed due to the sudden increase of temperature by burning of carbon. This sudden increase of temperature due to burning formed the filled NiO@void@NiO nanobelt as an intermediate product and ultimately the tube-in-tube nanobelt formed by Ostwald ripening [40,41]. The elemental mapping images shown in Fig. 4f reveal uniform distributions of Ni and O components all over the nanobelts. Carbon component was not observed due to complete combustion of carbon during the formation of NiO nanobelts with tube-in-tube structure.

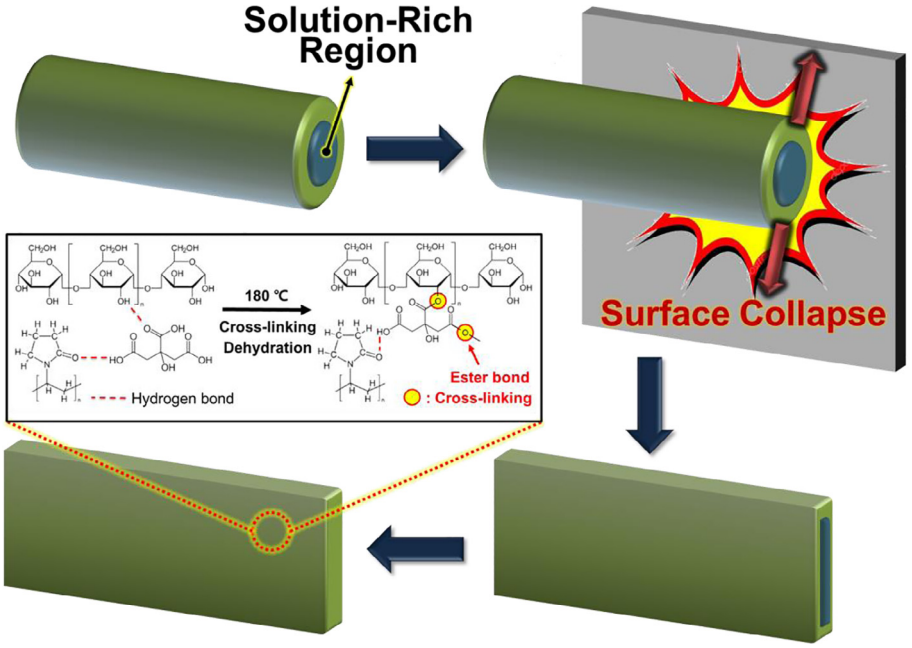

Scheme 1. Physical procedure and chemical explanations for the roles of PVP, dextrin, and citric acid in the formation of nanobelt structure during electrospinning process.

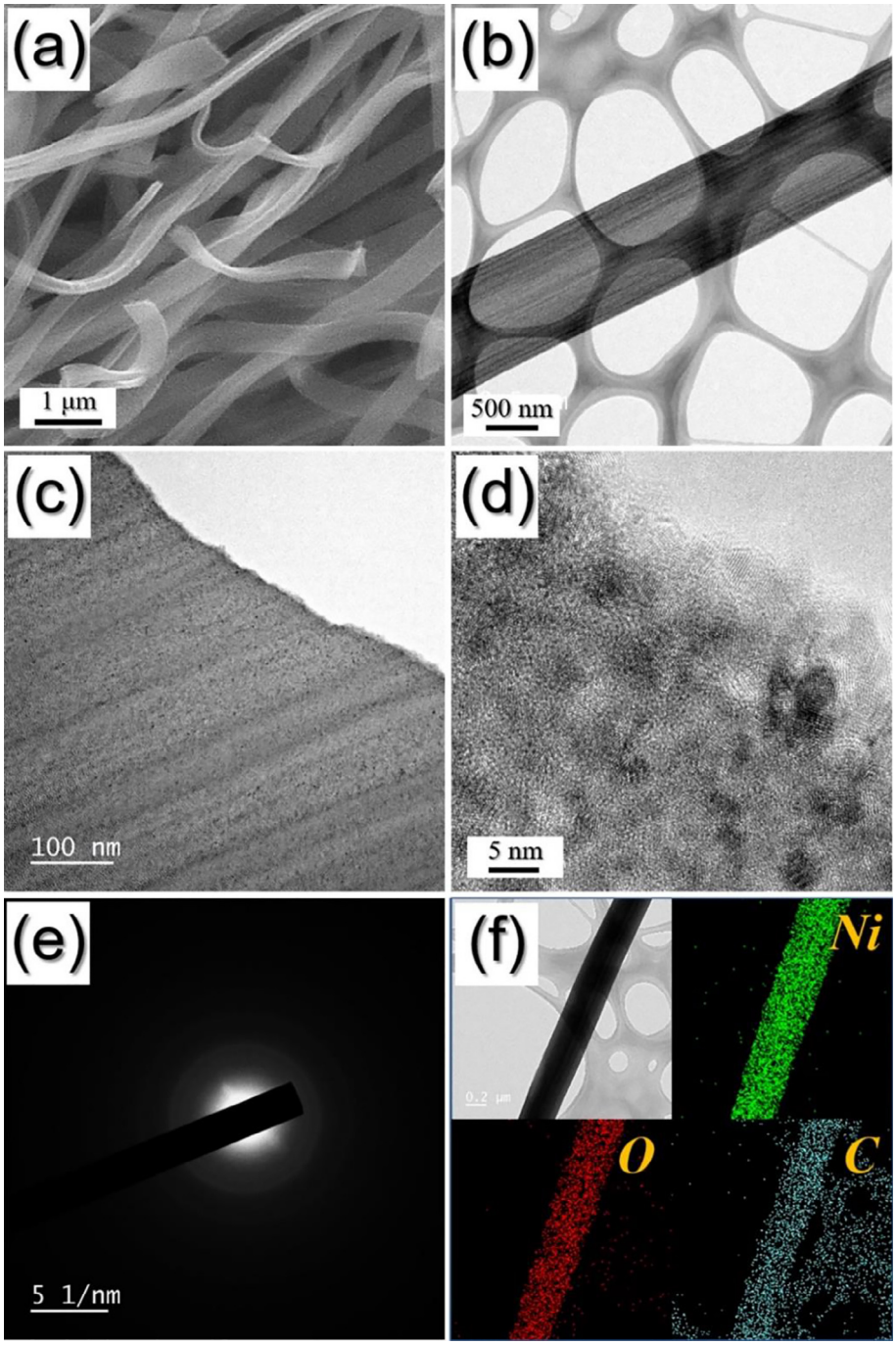

Fig. 3. Morphologies, SAED pattern, and elemental mapping images of NiO/C-300 nanobelts formed by oxidation process at 300 °C: (a) SEM image, (b, c) TEM images, (d) HR-TEM image, (e) SAED pattern, and (f) elemental mapping images.

Formation mechanism of the tube-in-tube structured NiO nanobelts is investigated in detail by tracing the morphological changes of the nanobelts induced by the post-treatments and is shown in Scheme 2. The carbonization of PVP, dextrin, and citric acid and decomposition of the nickel salt formed amorphous NiO–C composite nanobelts with filled structure. The combustion of outer layer carbon and oxidation of NiO resulted in the formation of NiO-C@NiO core-shell nanobelt. Subsequent contraction of inner part NiO-C composite nanobelts during combustion formed fiber-in-tube structured NiO-C@void@NiO nanobelts. When carbon in NiO-C fiber was removed, filled NiO@void@NiO intermediate nanobelt was formed. Continuous heating resulted in Ostwald ripening and formed hollow NiO inner tube. Consequently, tube-in-tube structured NiO nanobelts could be prepared via one-step post-treatment of the electrospun nanobelts as described in Scheme 2. As-spun nanobelt was calcined at 400 °C by changing the ramping rate (1 and 10 °C min^{-1}) to support the formation mechanism (Scheme 2) of NiO nanobelts with tube-in-tube structure (which was prepared at a ramping rate of 5 °C min^{-1}) and their SEM images are shown in Fig. S4. At a slow ramping rate of 1 °C/min, carbon in the composite nanobelt was slowly decomposed and therefore, porous structured NiO nanobelt was obtained in Fig. S4. However, at a high ramping rate of 10 °C/min, composite nanobelt was quickly heated resulting from the maximization of temperature gradient. Therefore, NiO nanoparticles nucleated near the belt surface and grew larger by Ostwald ripening and resulted in hollow nanobelt in Fig. S4. From the above results, ramping rate control during heat-treatment, along with temperature control, could

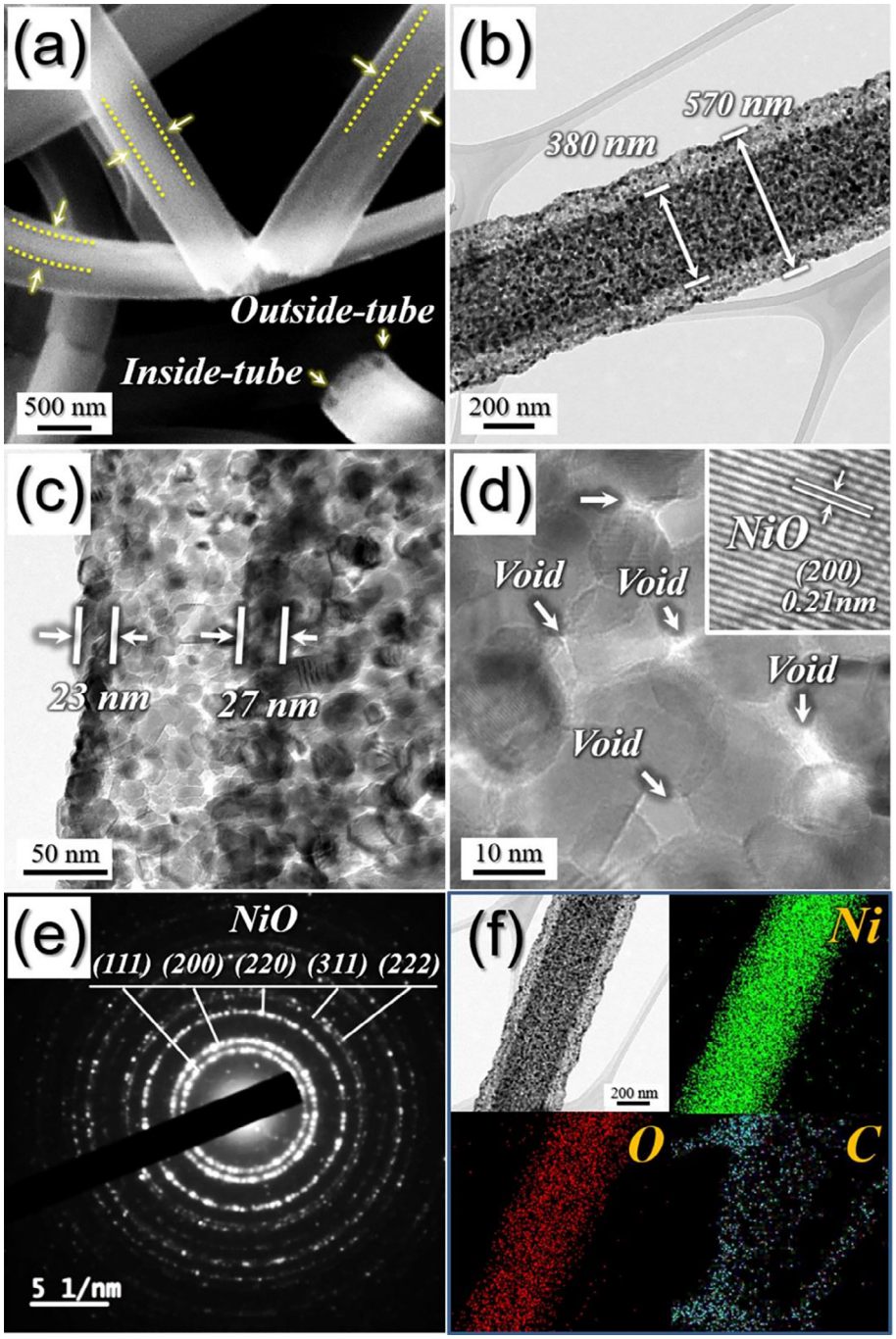

Fig. 4. Morphologies, SAED pattern, and elemental mapping images of NiO-400 nanobelts formed by oxidation process at 400 °C: (a) SEM image, (b, c) TEM images, (d) HR-TEM image, (e) SAED pattern, and (f) elemental mapping images.

be an important factor to prepare the tube-in-tube structured NiO.

The chemical nature of the NiO nanobelts (NiO/C-300, NiO-400, and NiO-500) was analyzed by XPS as shown in Fig. S5. Survey scan in Fig. S5a revealed the peaks that confirmed the existence of Ni and O elements. C 1s peak intensity was very high for NiO/C-300 as can be seen in Fig. S5a, but was not observed elsewhere (Fig. S5b and S5c). Also, the intensity of Ni 2p peaks for NiO/C-300 were very low, compared to those of NiO-400, and NiO-500 nanobelts due to the existence of carbon at the surface. Ni 2p spectrum shown in Fig. S5d-f revealed peaks at 853.1 and 872.1 eV that correspond to Ni^{2+} [46,47]. Furthermore, XPS peak at 855.8 eV labelled as Surface + Non-local peak, which is relevant to the pyramidally coordinated Ni atoms near nickel oxide surface, was observed in NiO-400 and NiO-500 as shown in Fig. S5e-f. The Surface + Non-local peak was not observed in NiO/C-300, presumably due to the low oxidation temperature. O 1s spectra revealed two peaks at 529.4 and 531.2 eV corresponding to O-Ni (II) bond and low coordination numbered oxygen ions at the surface, respectively [46,47].

As the oxidation temperature increased to 500 °C under an air atmosphere, the nanobelt did not retain tube-in-tube structure due to the densification and sintering occurring at high treatment temperature, as can be seen in the SEM and TEM images in Fig. 5. SEM image in Fig. 5a shows nanobelts with bumpy surface. The TEM images shown in Fig. 5b, c reveal the nanofiber consisting of well-faceted dense NiO crystals. Some of the pores with 15 nm in size present in the structures were observed in the TEM image in Fig. 5c. XRD pattern in Fig. S2

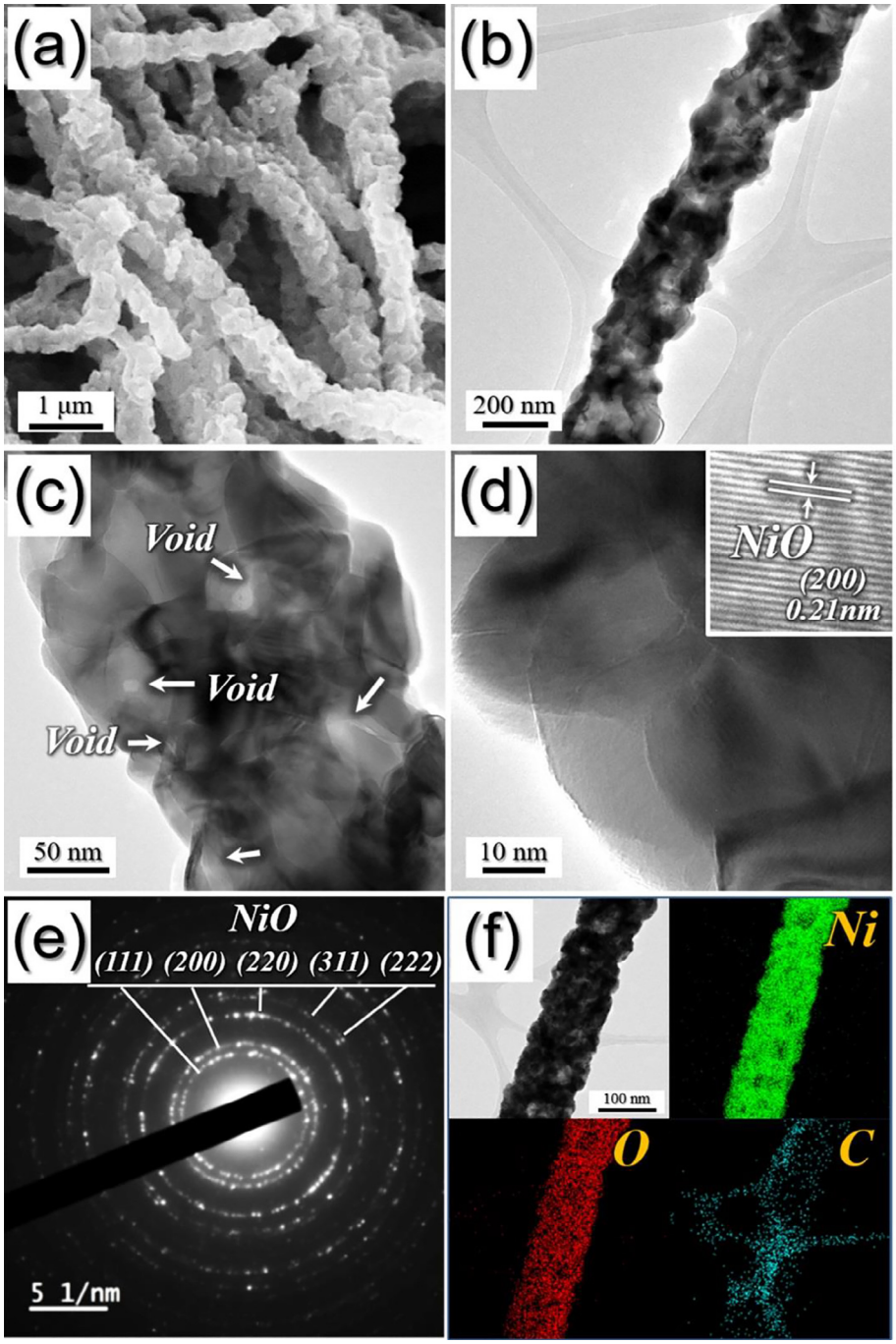

Fig. 5. Morphologies, SAED pattern, and elemental mapping images of NiO-500 nanobelts formed by oxidation process at 500 °C: (a) SEM image, (b, c) TEM images, (d) HR-TEM image, (e) SAED pattern, and (f) elemental mapping images.

exhibited NiO phase, and the mean crystallite size of NiO comprising NiO-500 was 36 nm. Fig. 5d clearly reveals the lattice fringes with an interplanar distance of 0.21 nm, which is in line with the (200) plane in the SAED pattern shown in Fig. 5e. The elemental mapping images of post-treated nanofibers at 500 °C showed good dispersion of Ni and O components in the nanobelts, as shown in Fig. 5f. The N_2 gas adsorption and desorption isotherms are presented in Fig. S6. The Brunauer-Emmett-Teller (BET) surface areas of NiO/C-300, NiO-400, and NiO-500 nanobelts post-treated at 300, 400, and 500 °C were 23, 47, and 21 $m^2 g^{-1}$, respectively. Tube-in-tube structured NiO-400 shows 2.1 and 2.3 times higher BET surface area than those of NiO/C-300 and NiO-500, respectively. Well-developed pores between nanocrystals led to a high BET surface area. Lower BET surfaces areas of NiO/C-300 and NiO-500 could be attributed to the dense structure of nanobelt containing carbon and crystal growth, respectively.

The electrochemical properties of NiO nanobelts with various morphologies are shown in Fig. 6. The cyclic voltammograms (CV) of the NiO nanobelts analyzed over potential range of 0.001–3.0 V (vs. Li/Li^+) for the first 5 cycles were obtained at a scan rate of 0.1 mV s^{-1}, as presented in Figs. 6a and S7. The CV curves for the samples without carbon, oxidized at 400 and 500 °C were analogous in shape. A sharp peak located at 0.43 V in the first cathodic scan reveals the formation of ultrafine metallic Ni nanoparticles reduced from nickel oxide [3,10,25,35]. For carbon-containing NiO/C-300, this peak was shifted to a higher potential (0.87 V). The voltage plateau of NiO/C-300 is different from those of NiO-400 and NiO-500 due to the existence of

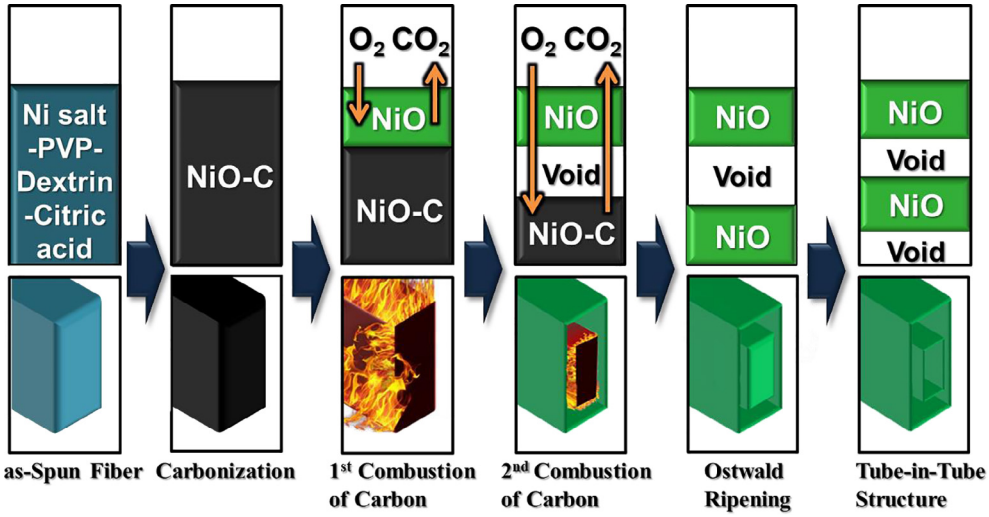

Scheme 2. Formation mechanism of NiO nanobelts with tube-in-tube structure prepared from oxidation of $Ni(NO_3)_2$-PVP-dextrin-citric acid composite nanobelts.

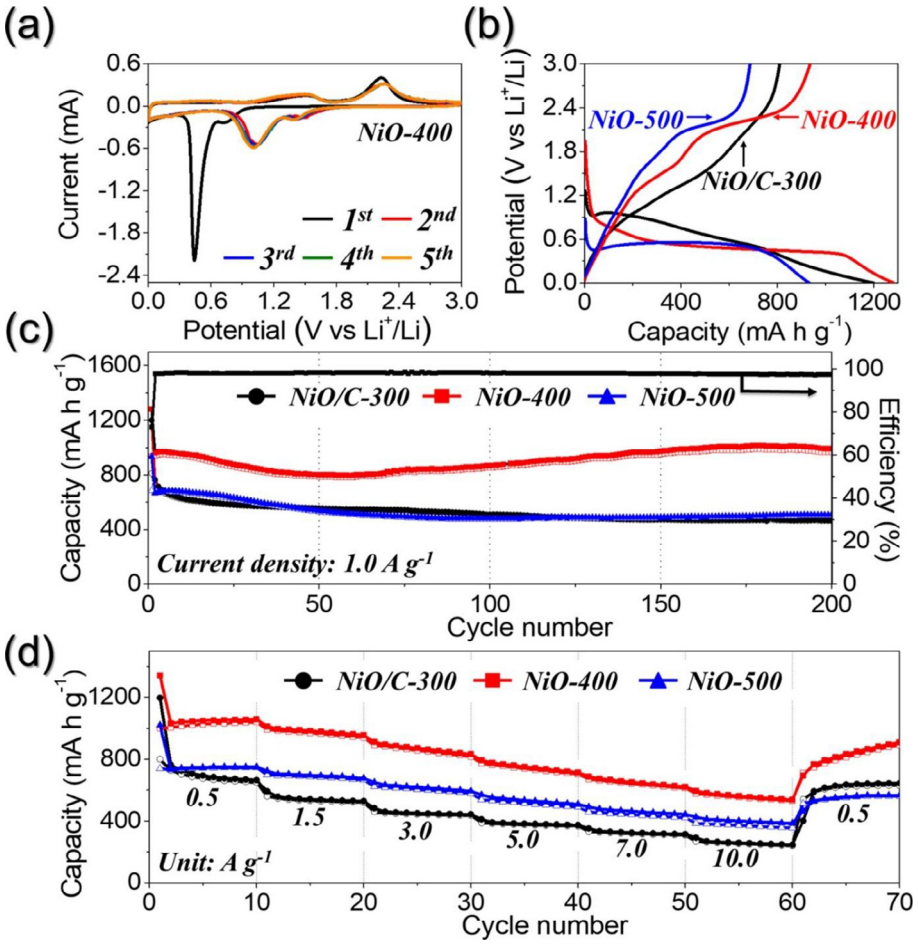

Fig. 6. Electrochemical properties of nanobelts post-treated at various temperatures: (a) CV curves of NiO-400, (b) initial charge and discharge profiles, and (c) cycle and (d) rate performances of NiO/C-300, NiO-400, and NiO-500 nanobelts.

carbon. The difference between the reduction and oxidation peaks (ΔV) of NiO/C-300 was smaller than those of NiO-400 and NiO-500, demonstrating the better conductivity and weaker polarization. This is due to the existence of carbon which is relatively conductive and beneficial for the lithium ion diffusion. Additionally, NiO/C-300 showed a long sloping tail corresponding to carbon intercalation process with Li^+ ion until the discharge step was terminated. Broad reduction peaks at 1.5, 0.74, and 0.6 V for NiO/C-300, NiO-400, and NiO-500 nanobelts were observed, which correspond to the partially reversible solid electrolyte interface (SEI) layer [20,31]. Peak intensity of NiO/C-300 was relatively very low in the first cycle because the nanobelt was composited with carbon material. The formation of ultrafine NiO nanocrystals triggered the shift in the location of main reduction and oxidation peaks from the second cycle onwards [48,49].

Two distinctive oxidation peaks were observed at 1.6 and 2.3 V, which correspond to the decomposition of SEI layer and oxidation of metallic Ni to Ni^{2+}, respectively [3,20,25,35]. The CV results during the 2^{nd}-5^{th} cycles overlapped well, indicative of excellent reversibility of the charge/discharge reactions. Fig. 6b shows the first initial charge/discharge curves of NiO nanobelts at a current density of 1.0 A g^{-1}. The plateaus coincided well with the CV results, firstly in way that NiO-400 exhibited plateaus at 0.74 and 0.43 V, respectively, during the first discharge process [50,51]. In the charge process, plateau at 2.3 V corresponding to the conversion of Ni metal to NiO further elucidate the consensus between the CV and the charge/discharge curves [50,51]. Cycling performance of the nanobelts at a high current density of 1.0 A g^{-1} is shown in Fig. 6c. The initial discharge capacities of NiO/C-300, NiO-400, and NiO-500 nanobelts were 953, 1282, and 935 mA h g^{-1}, respectively, and their initial Coulombic efficiencies were 68, 75, and 72%, respectively. Coulombic efficiency of NiO/C-300 was the lowest owing to the existence of carbon material with high irreversible capacity, whereas that of NiO-400 was the highest for its structural stability [44,45]. In case of NiO-500, lower Coulombic efficiency compared to that of NiO-400 can be attributed to the partial morphology destruction of the NiO nanobelt. The discharge capacities of NiO/C-300, NiO-400, and NiO-500 nanobelts after 200 cycles at a current density of 1.0 A g^{-1} were 468, 992, and 509 mA h g^{-1}, respectively. Tube-in-tube structured NiO nanobelts exhibited the highest discharge capacity and the most stable cycling performance among the samples. It was attributed to the existence of hollow space between shells, and void in the inside shell that allowed effective accommodation of volume changes during lithiation/delithiation, increasing the structural stability. The tube-in-tube nanobelt exhibited excellent rate performance, as shown in Fig. 6d. The hollow interior of the nanobelt played an important role in decreasing diffusion length, thus leading to improved Li^+ ion diffusion rate. The discharge capacities of the tube-in-tube nanobelt were 1058, 955, 832, 715, 612, and 531 mA h g^{-1} at the current density of 0.5, 1.5, 3.0, 5.0, 7.0, and 10.0 A g^{-1}, respectively. It is noteworthy that the nanobelt exhibited very high capacity at an extremely high current density of 10.0 A g^{-1}.

EIS was analyzed to investigate the reason for the excellent cycling and rate performances of tube-in-tube NiO nanobelt. The Nyquist plots of the nanobelts, which are characterized by the semicircles in medium-frequency region, are shown in Fig. 7 [52–55]. Nyquist plots were obtained by deconvolution with a Randle-type equivalent circuit model shown in Fig. S8. The electrochemical reaction types such as charge transfer reaction, lithium ion migration through SEI layers, and Li^+ ion diffusion kinetics in the active materials are described by the equivalent circuit model. The precise values of charge transfer resistance were obtained from the simulated equivalent circuit. Charge transfer resistance (R_{ct}) of the samples, calculated from the semicircles, were 97, 32, and 29 Ω before cycling, as shown in Fig. 7a. NiO/C-300 exhibited the highest R_{ct} value due to the amorphous NiO nanocrystals constituting the nanobelt [56]. R_{ct} values decreased after the first cycle due to the formation of ultrafine NiO nanocrystals [35,57]. NiO/C-300, NiO-400, and NiO-500 nanobelts exhibited R_{ct} values of 27, 18, and 21 Ω after 50 cycles, respectively. The R_{ct} value of NiO-400 was the lowest among the three nanobelts, which is an evidence of high structural stability of the tube-in-tube structure during the repeated lithiation and delithiation processes. The existence of hollow space between shells, and void in the inside shell improves the structure stability and allows numerous electrochemical reaction sites. Additionally, Li^+ ion diffusion length is decreased owing to the structural merits of tube-in-tube structure. These altogether lead to the excellent lithium-ion storage properties of tube-in-tube structured NiO nanobelts when applied as anode material for LIBs. In order to prove the structural merits of tube-in-tube nanofiber morphology, SEM images of NiO/C-300, NiO-400, and NiO-500 nanobelts after 50 cycles at a current density of 1.0 A g^{-1} were taken. In Fig. 8, tube-in-tube morphology maintained well after 50 cycles, proving its structural stability. NiO/C-300 nanobelt

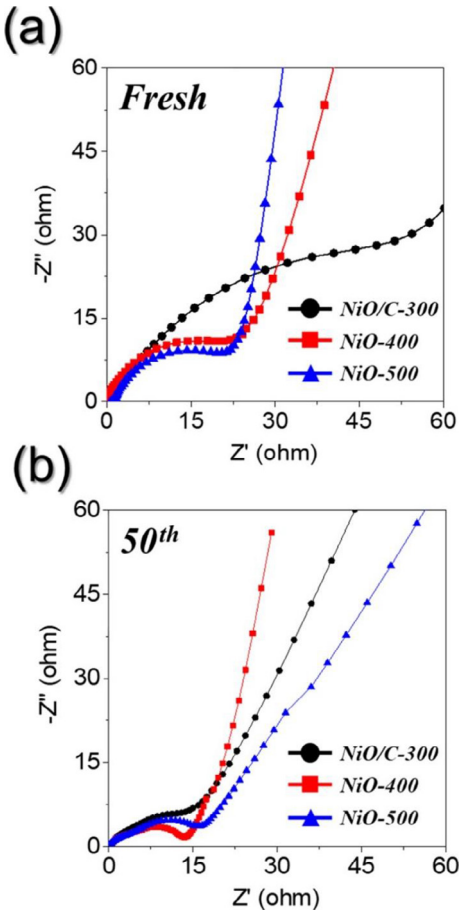

Fig. 7. Nyquist impedance plots of NiO/C-300, NiO-400 and NiO-500 nanobelts: (a) before cycling and (b) after 50^{th} cycle.

also maintained its morphology well, whereas broken pieces were observed in case of NiO-500 nanobelt. NiO-500 nanobelt structure was destroyed for the structure could not effectively alleviate the volume change during cycling. Table S1 lists previously reported NiO nanostructures synthesized from various preparation methods and their electrochemical properties, which are compared to those of NiO tube-in-tube nanobelts prepared by electrospinning process and subsequent one-step oxidation. Tube-in-tube structured nanobelt prepared in this study showed excellent electrochemical properties at a high current density of 1.0 A g^{-1} compared to other nanostructured NiO materials. This was attributed to the existence of hollow space between shells, and void in the inside shell with ability to effectively accommodate the volume changes during electrochemical cycling, which increased the structural stability. The hollow interior decreased diffusion length and improved Li^+ ion diffusion rate. In addition, the 1D structure enabled the electron transport along the longitudinal direction, additionally reducing Li^+ ion diffusion length, and increasing electrolyte/active material contact.

4. Conclusions

In this study, NiO nanobelts with tube-in-tube structure were prepared by post-treatment of electrospun $Ni(NO_3)_2$-PVP-dextrin-citric acid composite nanobelts under air atmosphere. PVP played bifunctional roles of increasing viscosity and lowering surface tension for electrospun nanobelts with high uniformity. Citric acid helped lower the surface tension and went through cross-linking process with dextrin, which is hygroscopic in nature. The sudden combustion of the carbonized PVP, dextrin, and citric acid was the key requirement to

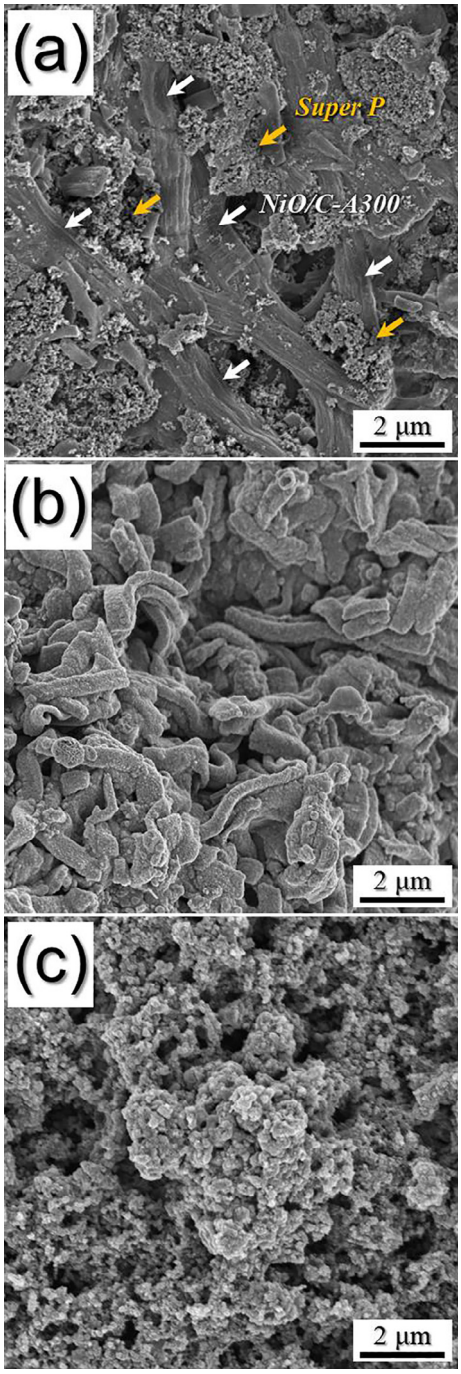

Fig. 8. SEM images of (a) NiO/C-300, (b) NiO-400, and (c) NiO-500 after 50 cycles at 1.0 A g^{-1}.

form intermediate NiO-C@void@NiO fiber-in-tube morphology. Further oxidation transformed inner NiO-C nanobelt into hollow NiO tube through Ostwald ripening process, and tube-in-tube structured NiO nanobelts were obtained. NiO nanobelts with a tube-in-tube structure exhibited superior Li-ion storage properties compared with filled NiO-C nanobelts and porous NiO nanobelts.

Acknowledgements

This research was supported by the Technology Development Program to Solve Climate Changes of the National Research Foundation (NRF) funded by the Ministry of Science, ICT & Future Planning (NRF-2017M1A2A2087577 and NRF-2017R1A4A1014806). This work was supported by the Energy Efficiency & Resources Core Technology Program of the Korea Institute of Energy Technology Evaluation and Planning (KETEP), granted financial resource from the Ministry of Trade, Industry & Energy, Republic of Korea (20153030091450).

Appendix A. Supplementary data

Supplementary data associated with this article can be found, in the online version, at http://dx.doi.org/10.1016/j.cej.2018.04.156.

References

[1] M.Y. Son, Y.J. Hong, Y.C. Kang, Superior electrochemical properties of Co_3O_4 yolk–shell powders with a filled core and multishells prepared by a one-pot spray pyrolysis, Chem. Commun. 49 (2013) 5678–5680.
[2] L. Xia, S. Wang, G. Liu, L. Ding, D. Li, H. Wang, S. Qiao, Flexible SnO_2/N-doped carbon nanofiber films as integrated electrodes for lithium-ion batteries with superior rate capacity and long cycle life, Small 12 (2016) 853–859.
[3] C. Chen, N. Ding, L. Wang, Y. Yu, I. Lieberwirth, Some new facts on electrochemical reaction mechanism for transition metal oxide electrodes, J. Power Sources 189 (2009) 552–556.
[4] J. Qu, Y.-X. Yin, Y.-Q. Wang, Y. Yan, Y.G. Guo, I. Lieberwirth, W.-G. Song, Layer structured α-Fe_2O_3 nanodisk/reduced graphene oxide composites as high-performance anode materials for lithium-ion batteries, ACS Appl. Mater. Interfaces 5 (2013) 3932–3936.
[5] P. Poizot, S. Laruelle, S. Grugeon, L. Dupont, J.-M. Tarascon, Nano-sized transition-metal oxides as negative-electrode materials for lithium-ion batteries, Nature 407 (2000) 496–499.
[6] M.S. Balogun, Z. Wu, Y. Luo, W. Qiu, X. Fan, B. Long, M. Huang, P. Liu, Y. Tong, High power density nitridated hematite (α-Fe_2O_3) nanorods as anode for high-performance flexible lithium ion batteries, J. Power Sources 308 (2016) 7–17.
[7] Q. An, F. Lv, Q. Liu, C. Han, K. Zhao, J. Sheng, Q. Wei, M. Yan, L. Mai, Amorphous vanadium oxide matrixes supporting hierarchical porous Fe_3O_4/graphene nanowires as a high-rate lithium storage anode, Nano Lett. 14 (2014) 6250–6256.
[8] H. Cheng, C.Y. Su, Z.Y. Tan, S.Z. Tai, Z.Q. Liu, Interacting $ZnCo_2O_4$ and Au nanodots on carbon nanotubes as highly efficient water oxidation electrocatalyst, J. Power Sources 357 (2017) 1–10.
[9] W. Qiu, M.S. Balogun, Y. Luo, K. Chen, Y. Zhu, X. Xiao, X. Lu, P. Liu, Y. Tong, Three-dimensional Fe_3O_4 nanotube array on carbon cloth prepared from a facile route for lithium ion batteries, Electrochim. Acta 193 (2016) 32–38.
[10] Y.J. Mai, S.J. Shi, D. Zhang, Y. Lu, C.D. Gu, J.P. Tu, NiO–graphene hybrid as an anode material for lithium ion batteries, J. Power Sources 204 (2012) 155–161.
[11] Z. Liang, R. Huo, Y.X. Yin, F. Zhang, S. Xu, Y.G. Guo, Carbon-supported Ni@NiO/Al_2O_3 integrated nanocomposite derived from layered double hydroxide precursor as cycling-stable anode materials for lithium-ion batteries, Electrochim. Acta 108 (2013) 429–434.
[12] D. Su, M. Ford, G. Wang, Mesoporous NiO crystals with dominantly exposed {110} reactive facets for ultrafast lithium storage, Sci. Rep. 2 (2012) 924.
[13] B. Varghese, M.V. Reddy, Z. Yanwu, C.S. Lit, T.C. Hoong, G.V. Subba Rao, B.V.R. Chowdari, A.T.S. Wee, C.T. Lim, C.-H. Sow, Fabrication of NiO nanowall electrodes for high performance lithium ion battery, Chem. Mater. 20 (2008) 3360–3367.
[14] S.W. Oh, H.J. Bang, Y.C. Bae, Y.-K. Sun, Effect of calcination temperature on morphology, crystallinity and electrochemical properties of nano-crystalline metal oxides (Co_3O_4, CuO, and NiO) prepared via ultrasonic spray pyrolysis, J. Power Sources 173 (2007) 502–509.
[15] H. Wang, L.-F. Cui, Y. Yang, H. Sanchez Casalongue, J.T. Robinson, Y. Liang, Y. Cui, H. Dai, Fabrication of NiO nanowall electrodes for high performance lithium ion battery, J. Am. Chem. Soc. 132 (2010) 13978–13980.
[16] Z. Wang, L. Zhou, X.W.D. Lou, Metal oxide hollow nanostructures for lithium-ion batteries, Adv. Mater. 24 (2012) 1903–1911.
[17] X. Jia, Z. Chen, X. Cui, Y. Peng, X. Wang, G. Wang, F. Wei, Y. Lu, Building robust architectures of carbon and metal oxide nanocrystals toward high-performance anodes for lithium-ion batteries, ACS Nano 6 (2012) 9911–9919.
[18] S.H. Choi, Y.C. Kang, Ultrafast synthesis of yolk-shell and cubic NiO nanopowders and application in lithium ion batteries, ACS Appl. Mater. Interfaces 6 (2014) 2312–2316.
[19] X.H. Huang, J.P. Tu, B. Zhang, C.Q. Zhang, Y. Li, Y.F. Yuan, H.M. Wu, Electrochemical properties of NiO–Ni nanocomposite as anode material for lithium ion batteries, J. Power Sources 161 (2006) 541–544.
[20] J.S. Cho, J.M. Won, J.-H. Lee, Y.C. Kang, Synthesis and electrochemical properties of spherical and hollow-structured NiO aggregates created by combining the Kirkendall effect and Ostwald ripening, Nanoscale 7 (2015) 19620–19626.
[21] S.H. Choi, Y.N. Ko, J.-K. Lee, Y.C. Kang, Rapid continuous synthesis of spherical reduced graphene ball-nickel oxide composite for lithium ion batteries, Sci. Rep. 4 (2014) 5786.
[22] X. Wang, Z. Yang, X. Sun, X. Li, D. Wang, P. Wang, D. He, NiO nanocone array electrode with high capacity and rate capability for Li-ion batteries, J. Mater. Chem. 21 (2011) 9988–9990.
[23] C. Wang, D. Wang, Q. Wang, H. Chen, Fabrication and lithium storage performance of three-dimensional porous NiO as anode for lithium-ion battery, J. Power Sources 195 (2010) 7432–7437.

[24] X.H. Huang, J.P. Tu, X.H. Xia, X.L. Wang, J.Y. Xiang, L. Zhang, Y. Zhou, Morphology effect on the electrochemical performance of NiO films as anodes for lithium ion batteries, J. Power Sources 188 (2009) 588–591.
[25] H.S. Jadhav, G.M. Thorat, J. Mun, J.G. Seo, Self-assembled hierarchical 3D – NiO microspheres with ultra-thin porous nanoflakes for lithium-ion batteries, J. Power Sources 302 (2016) 13–21.
[26] H. Liu, G. Wang, J. Liu, S. Qiao, H. Ahn, Highly ordered mesoporous NiO anode material for lithium ion batteries with an excellent electrochemical performance, J. Mater. Chem. 21 (2011) 3046–3052.
[27] L. Wu, X. Hu, J. Qian, F. Pei, F. Wu, R. Mao, X. Ai, H. Yang, Y. Cao, Sb–C nanofibers with long cycle life as an anode material for high-performance sodium-ion batteries, Energy Environ. Sci. 7 (2014) 323–328.
[28] J. Tian, Z. Zhao, A. Kumar, R.I. Boughton, H. Liu, Recent progress in design, synthesis, and applications of one-dimensional TiO_2 nanostructured surface heterostructures: a review, Chem. Soc. Rev. 43 (2014) 6920–6937.
[29] J.S. Cho, Y.J. Hong, Y.C. Kang, Design and synthesis of bubble-nanorod-structured Fe_2O_3–carbon nanofibers as advanced anode material for Li-ion batteries, ACS Nano 9 (2015) 4026–4035.
[30] J.L. Xie, C.X. Guo, C.M. Li, Construction of one-dimensional nanostructures on graphene for efficient energy conversion and storage, Energy Environ. Sci. 7 (2014) 2559–2579.
[31] M.S. Balogun, W. Qiu, Y. Luo, Y. Huang, H. Yang, M. Li, M. Yu, C. Liang, P. Fang, P. Liu, Y. Tong, Improving the lithium-storage properties of self-grown nickel oxide: a back-up from TiO_2 nanoparticles, ChemElectroChem 2 (2015) 1243–1248.
[32] M.S. Balogun, Y. Huang, W. Qiu, H. Yang, H. Ji, Y. Tong, Updates on the development of nanostructured transition metal nitrides for electrochemical energy storage and water splitting, Mater. Today 20 (2017) 425–451.
[33] X. Yu, Y. Fu, X. Cai, H. Kafafy, H. Wu, M. Peng, S. Hou, Z. Lv, S. Ye, D. Zou, Flexible fiber-type zinc–carbon battery based on carbon fiber electrodes, Nano Energy 2 (2013) 1242–1248.
[34] C. Zhu, X. Mu, P.A. van Aken, Y. Yu, J. Maier, Single-layered ultrasmall nanoplates of MoS_2 embedded in carbon nanofibers with excellent electrochemical performance for lithium and sodium storage, Angew. Chem. Int. Ed. 53 (2014) 2152–2156.
[35] J.S. Cho, S.Y. Lee, H.S. Ju, Y.C. Kang, Synthesis of NiO nanofibers composed of hollow nanospheres with controlled sizes by the nanoscale Kirkendall diffusion process and their electrochemical properties, ACS Appl. Mater. Interfaces 7 (2015) 25641–25647.
[36] N. Yuya, W. Kai, B. Kim, I. Kim, Morphology controlled electrospun poly (vinyl pyrrolidone) fibers: effects of organic solvent and relative humidity, J. Mater. Sci. Technol. 2 (2010) 97–112.
[37] S. Chuangchote, T. Sagawa, S. Yoshikawa, Electrospinning of poly (vinyl pyrrolidone): effects of solvents on electrospinnability for the fabrication of poly (*p*-phenylene vinylene) and TiO_2 nanofibers, J. Appl. Polym. Sci. 114 (2009) 2777–2791.
[38] M. Hoorfar, M.A. Kurz, Z. Policova, M.L. Hair, A.W. Neumann, Do polysaccharides such as dextran and their monomers really increase the surface tension of water? Langmuir 22 (2006) 52–56.
[39] S. Mahiuddin, B. Minofar, J.M. Borah, M.R. Das, P. Jungwirth, Propensities of oxalic, citric, succinic, and maleic acids for the aqueous solution/vapour interface: surface tension measurements and molecular dynamics simulations, Chem. Phys. Lett. 462 (2008) 217–221.
[40] S. Koombhongse, W. Liu, D.H. Reneker, Flat polymer ribbons and other shapes by electrospinning, J. Polym. Sci. Pol. Phys. 39 (2001) 2598–2606.
[41] C. Huang, S. Chen, C. Lai, D.H. Reneker, H. Qiu, Y. Ye, H. Hou, Electrospun polymer nanofibres with small diameters, Nanotechnology 17 (2006) 1558.
[42] C. Menzel, E. Olsson, T.S. Plivelic, R. Andersson, C. Johansson, R. Kuktaite, L. Järnström, K. Koch, Molecular structure of citric acid cross-linked starch films, Carbohyd. Polym. 96 (2013) 270–276.
[43] N. Reddy, Y. Yang, Citric acid cross-linking of starch films, Food Chem. 118 (2010) 702–711.
[44] J.S. Cho, Y.J. Hong, Y.C. Kang, Electrochemical properties of fiber-in-tube- and filled-structured TiO_2 nanofiber anode materials for lithium-ion batteries, Chem. Eur. J. 21 (2015) 11082–11087.
[45] Y.J. Hong, J.H. Kim, Y.C. Kang, Sodium-ion storage performance of hierarchically structured $(Co_{1/3}Fe_{2/3})Se_2$ nanofibers with fiber-in-tube nanostructures, J. Mater. Chem. A 4 (2016) 15471–15477.
[46] A.G. Marrani, V. Novelli, S. Sheehan, D.P. Dowling, D. Dini, Probing the redox states at the surface of electroactive nanoporous NiO thin films, ACS Appl. Mater. interfaces 6 (2013) 143–152.
[47] W. Liu, C. Lu, X. Wang, K. Liang, B.K. Tay, *In situ* fabrication of three-dimensional, ultrathin graphite/carbon nanotube/NiO composite as binder-free electrode for high-performance energy storage, J. Mater. Chem. A 3 (2015) 624–633.
[48] H.J. Liu, S.H. Bo, W.J. Cui, F. Li, C.X. Wang, Y.Y. Xia, Nano-sized cobalt oxide/mesoporous carbon sphere composites as negative electrode material for lithium-ion batteries, Electrochim. Acta 53 (2008) 6497–6503.
[49] B.K. Zou, Y.Y. Zhang, J.Y. Wang, X. Liang, X.H. Ma, C.H. Chen, Hydrothermally enhanced MnO/reduced graphite oxide composite anode materials for high performance lithium-ion batteries, Electrochim. Acta 167 (2015) 25–31.
[50] C. Liu, C. Li, K. Ahmed, Z. Mutlu, C.S. Ozkan, M. Ozkan, Template free and binderless NiO nanowire foam for Li-ion battery anodes with long cycle life and ultrahigh rate capability, Sci. Rep. 6 (2016) 29813.
[51] J. Ma, L. Yin, T. Ge, 3D hierarchically mesoporous Cu-doped NiO nanostructures as high-performance anode materials for lithium ion batteries, CrystEngComm 17 (2015) 9336–9347.
[52] J.S. Cho, J.S. Park, Y.C. Kang, Preparation of Hollow Fe_2O_3 nanorods and nanospheres by nanoscale Kirkendall diffusion, and their electrochemical properties for use in lithium-ion batteries, Sci. Rep. 6 (2016) 38933.
[53] K. Lee, S.Y. Shin, Y.S. Yoon, Fe_3O_4 nanoparticles on MWCNTs backbone for lithium ion batteries, J. Korean Ceram. Soc. 53 (2016) 376–380.
[54] J.S. Park, Y.C. Kang, Multicomponent (Mo, Ni) metal sulfide and selenide microspheres with empty nanovoids as anode materials for Na-ion batteries, J. Mater. Chem. A 5 (2017) 8616–8623.
[55] S.F. Zhang, W.P. Wang, S. Xin, H. Ye, Y.X. Yin, Y.G. Guo, Graphitic nanocarbon–selenium cathode with favorable rate capability for Li–Se batteries, ACS Appl. Mater. Interfaces 9 (2017) 8759–8765.
[56] J. Ma, X. Zhang, K. Chen, G. Li, X. Han, Morphology-controlled synthesis of hematite hierarchical structures and their lithium storage performances, J. Mater. Chem. A 1 (2013) 5545–5553.
[57] Y. Sun, X. Hu, W. Luo, F. Xia, Y. Huang, Reconstruction of conformal nanoscale MnO on graphene as a high-capacity and long-life anode material for lithium ion batteries, Adv. Funct. Mater. 23 (2013) 2436–2444.